Simulating Material Deposit for Fiber Sprayed Composites using Beta Paint Distribution

Fabian Viessmann[1], Lukas Wagner[2], Georg Puchas[2], Stefan Schafföner[2], and Dominik Henrich[1]

[1] University of Bayreuth, Chair for Robotics and Embedded Systems, D-95440 Bayreuth, Germany,
fabian.viessmann@uni-bayreuth.de

[2] University of Bayreuth, Chair of Ceramic Materials Engineering (CME), D-95440 Bayreuth, Germany

Abstract. Fiber reinforced composites are often manufactured using cost-effective fiber spraying processes. As quality fluctuates during manual manufacturing, a robot-based automation is advantageous. The automation could be greatly improved by a prior simulation of the material deposit to minimize overspray and to ensure a homogeneous material distribution. Even so, currently, specific simulation models for fiber spraying processes are unavailable. Thus, this paper investigates in which respect existing spraying process models are able to predict the material deposit, as they do not include variables such as fibers and compressed air. As a use case, we consider a thermal spraying model for the manufacturing of short fiber reinforced oxide fiber composites. We evaluate the model by simulating the deposit on a planar workpiece. The evaluation reveals that this model can only be applied to a limited extent. For higher accuracy, the model must consider further fiber spraying characteristics.

Keywords: Simulation, Material deposit, Fiber spraying process, Fiber sprayed composites, Industrial robotics, Beta paint distribution

1 Introduction

Fiber reinforced composites are lightweight materials that offer valuable properties, such as a high strength-to-weight ratio, fatigue resistance, and design flexibility [1]. Accordingly, these materials are becoming increasingly important and are used today in numerous fields, such as energy, automotive, space and aeronautics or civil engineering [2]. Often they are manufactured by a *fiber spraying process* (FSP) since an FSP is flexible and cost-effective [3]. Widely established examples are glass fiber composites [4] and recently also ceramic matrix composites, such as *oxide fiber composites* (OFC) [5]. However, these processes have traditionally been carried out manually, leading to a larger variability of the composite quality. As a result, robotic automation has been the focus of research in recent years to improve production costs, throughput, accuracy and reproducibility [3].

In order to obtain ceramic matrix composites with damage tolerant fracture behavior, the coating thickness during spraying must be as homogeneous as possible. Furthermore, to reduce material waste, the amount of material that does not reach the surface of the mold or does not provide any functionality must be minimized (*overspray*). Therefore, the robot must be programmed to fulfill these two criteria. For example, the fulfillment can be achieved by an expensive trial-and-error strategy. However, a simulation of the material deposit resulting from a robot trajectory before the manufacturing can greatly improve the cost-efficiency.

In this paper, we examine the extent to which the material deposit can be predicted in a robot-based FSP using existing models for spraying processes in general. We consider our automation approach for the manufacturing of short fiber reinforced OFC [5] as a use case, in which the programming is based on the intuitive playback programming paradigm [6]. For our automation approach, we therefore apply an existing simulation model used for thermal spraying [7]. As our approach utilizes pressure regulators, we extend the model to include compressed air influence. The goal is to investigate the applicability of the model in terms of the accuracy of the simulated deposit. For an FSP, the deposit mainly consists of fibers which are not taken into account by prior models explicitly. Therefore, Sec. 2 gives an overview of the related work regarding the automation of FSPs and simulation models for spraying processes. In Sec. 3, we explain the concrete model and its application to our FSP, taking compressed air into account. In Sec. 4, we evaluate the model in terms of the accuracy of the simulated thickness. At the end, Sec. 5 summarizes and concludes our paper.

2 Related Work

Fiber spraying systems are widely commercially available [8,9,10]. However, most of them have to be operated manually like a spray paint gun, which exposes the operator to air pollution. Furthermore, the result is not reproducible and very error-prone. A robot-based automation would overcome these disadvantages.

To the best of our knowledge, there are only two robot-based FSPs. One approach uses off-line programming, which combines graphical programming and virtual reality. The system has a two-axis turntable for greater flexibility [11]. However, this programming framework is not suitable for small batch sizes since it requires experts in robot programming. In our automation approach for manufacturing short fiber reinforced OFC, non-experts program the robot using the intuitive playback programming paradigm [5]. Therefore, the programming consists of two phases [6]. First, the operator guides the robot kinesthetically while the robot configurations are recorded at a constant frequency. Subsequently, the robot program can be played back and edited intuitively [12]. Our approach also uses a two-axis turntable for better flexibility and can be extended to other kinds of FSPs, like glass fiber spraying [5].

Both approaches do not simulate the material deposit before the manufacturing, so that there is no simulation model for FSPs available. Therefore, we

consider other general spraying process models. These models are divided into microscopic and macroscopic models [7]. Microscopic models deal with the simulation at the particle level, while macroscopic models abstract from individual particles and consider mass flow. Since it is sufficient for us to consider the mass flow, and since this is possible in a short computing time, we will only deal with this type of model. An overview of robot spray painting models is given by Chen et al. [13].

For simplified situations with a constant spraying distance, orthogonal spraying, and a planar workpiece, modeling the material distribution is sufficient. Thus, the first models describe this distribution by summing several Gaussian functions [14,15]. Less complex is the beta distribution model, which allows a clear choice of parameters depending on the spray gun [16,17] and which has been extended to 2D [18]. In order to predict the material deposit on curved surfaces, a deposition model plane is utilized which also considers different spraying distances and angles [14,19,20]. Previously, a comparable model was employed that predicted thermal spraying processes well [7].

In summary, there are many models available for material deposit simulations. However, it is still an open question whether these can be applied to an FSP. They also do not consider the influence of fibers and the compressed air. To fill this gap, we are investigating the applicability of the thermal spraying model [7] to our FSP and extend it in terms of the compressed air influence.

3 Methodology

We aim to predict the material deposit on the workpiece as part of our FSP for OFC [5] by applying an existing simulation model. In such an FSP, continuous oxide fiber bundles (roving) are chopped to uniform length by a cutting unit and then ejected out of the spray gun into a slurry spray. The fiber bundles are infiltrated with the slurry during the flight. Immediately afterwards, the fiber slurry mixture reaches the surface of a mold [21]. The resulting thickness results primarily from the fibers and secondarily from the slurry.

The thickness depends on the *robot trajectory* defined as a sequence $\mathcal{C} = (q_0, q_1, \ldots, q_n)$ of joint configurations $q_i \in \mathbb{R}^d$ with d joints of the robot at each timestep i. A joint configuration q_i is transformed into the *tool center point* (TCP) $p_i \in \mathbb{R}^3$ in workspace by using the forward kinematics of the robot. It is assumed that the TCP lies directly in front of the spray gun nozzle and represents the apex of an *elliptic spray cone*. The spray cone has an axis a_i that points into the interior of the cone. Furthermore, to control the material flow and the spray pattern, we use five pressure regulators [6]. The *round jet* and *flat jet* influence the elliptic spray pattern, while the *slurry value* defines the slurry volume flow. The *pilot air* serves for the de-/activation of the material flow ejected out of the spray gun, and the *cutter value* influences the compressed air that controls the cutting unit speed. For the simulation, we only consider the influence of different round and flat jet values. The slurry value is assumed to be constant, as this does not influence the fiber deposit. The pilot air is assumed

to be activated, while the cutter value for a uniform fiber length is also assumed to be greater than zero and constant. Thus, we define the round jet value as p_r and the flat jet value as p_f, which are constant for all timesteps.

To simulate the material deposit, a CAD model of the workpiece must be available. As for the thermal spraying model [7], we use a triangular mesh. This allows us to store the material deposit at each vertex. So our workpiece $\mathcal{W} = (V, F)$ is a set of vertices $V = \{v_0, v_1, \ldots, v_m\}$ with $v_j \in \mathbb{R}^3$ and faces $F \subset V^3$. Each vertex v_j has an associated normal n_j and all faces must have a consistent anti-clockwise orientation. Since we store the material deposit at the vertices v_j, we assume that the nodes v_j are uniformly distributed and close to each other, which is a requirement for a precise simulation.

3.1 Footprint Concept

For our FSP, we apply a simulation model used for thermal spraying [7], which utilizes a so-called *footprint*. A footprint describes the material distribution in the spray cone and can later be used to calculate the final material deposit on the workpiece. The footprint is determined by spraying orthogonally with a fixed position and orientation of the spray gun onto a flat surface for a given duration, distance to the workpiece, and pressure values. The material distribution of this footprint is determined by sampling the thicknesses, which, in our case, mainly consists of fibers compared to thermal spraying [7].

Generally, the footprint is modeled using a deposition model plane, called *footprint plane*, which is orthogonal to the axis a_i of the spray cone and shifted from the TCP by an offset λ in the direction of a_i. The shift by λ can be chosen arbitrarily, as this only scales the distribution in the footprint plane. The plane has its own coordinate system, where the intersection of a_i and the plane defines the origin. The x- and y-axis correspond to the half-axes of the elliptical spray pattern and depend on the spray gun. In the following, we call them $x_F, y_F \in \mathbb{R}^3$ defined in workspace. The footprint plane is shown in Fig. 1.

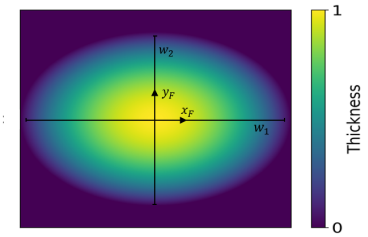

Fig. 1: An exemplary footprint plane with normalized deposit is shown here. The plane has its own coordinate system, whereby the origin is the intersection between the spray cone axis a_i and the plane. The two axes x_F and y_F are also the half-axes of the elliptical spray pattern. Within this plane, the spray cone has a diameter of w_1 along x_F and w_2 along y_F.

While the thermal spraying model [7] uses a sum of Gaussian distributions to describe the material distribution, we use a *bivariate beta paint distribution* [18]. The beta paint distribution is sufficient for us, as we assume that our distribution is unimodal and not rotated by any covariances. Furthermore, we modify it slightly so that the material deposit outside the spray cone is zero and that two diameters describe the spray cone size. The formula is given in Eq. 1.

$$T_{C,\beta_1,\beta_2,w_1,w_2}(x,y) = \begin{cases} C \cdot (1 - \frac{4x^2}{w_1^2})^{\beta_1 - 1} \cdot (1 - \frac{4y^2}{w_2^2 \cdot (1 - \frac{4x^2}{w_1^2})})^{\beta_2 - 1}, & \frac{4x^2}{w_1^2} + \frac{4y^2}{w_2^2} < 1 \\ 0, & \frac{4x^2}{w_1^2} + \frac{4y^2}{w_2^2} \geq 1 \end{cases} \tag{1}$$

Therefore, the thickness $T_{C,\beta_1,\beta_2,w_1,w_2}(x,y)$ at point $(x,y)^T$ in footprint coordinates depends on the following parameters: maximum thickness C, the shaping parameters β_1 and β_2, and the diameters w_1 and w_2 of the spray pattern within the footprint plane in x_F-/y_F-direction. In the following, the distribution is abbreviated as $T(x,y)$ if an explicit specification of the parameters is not necessary.

At this point, we extend the footprint concept to model the influence of p_r and p_f. Therefore, we determine our so-called *default footprint* with a fixed round and flat jet. This footprint has the parameters $\hat{C}, \hat{\beta}_1, \hat{\beta}_2, \hat{w}_1, \hat{w}_2$. When the round and flat jet change, we scale the default footprint to obtain a new distribution with the parameters $C, \beta_1, \beta_2, w_1, w_2$. Thus, we calculate new diameters by functions $w_1 = f(p_r, p_f)$ and $w_2 = g(p_r, p_f)$. These functions are defined for our spray gun in Sec. 3.4. To maintain the shape of the distribution, we set $\beta_1 = \hat{\beta}_1$ and $\beta_2 = \hat{\beta}_2$.

However, as the sum of the material deposit remains constant for all possible footprints, we must calculate a new maximum thickness C. Therefore, we choose C so that the sum of the material deposit is always equal to the sum of the material deposit of the default footprint, as the amount of mass flow does not change. Let I_d be the integral value of our default footprint and I_s the integral value of our scaled footprint. We determine the parameter C as given in Eq. 2.

$$C = \frac{I_d}{I_s} \cdot \hat{C} \tag{2}$$

3.2 Simulation model

Using the footprint plane, we calculate the material deposits at each vertex $v_j \in \mathcal{V}$. This calculation is heavily based on the thermal spraying model [7]. Therefore, we have to sum up the individual material deposits resulting from each robot configuration $q_i \in \mathcal{C}$ for a surface point $v_j \in \mathcal{V}$. Given a robot configuration q_i with corresponding TCP p_i, the spray direction is calculated by $d_{i,j} = v_j - p_i$. The material deposit at point v_j is determined by projecting point v_j onto the footprint plane along the spray direction $-d_{i,j}$ with corresponding

coordinates $(\pi_x(p_i, d_{i,j}), \pi_y(p_i, d_{i,j}))^T$. We calculate these as given in Eq. 3.

$$\pi_x(p_i, d_{i,j}) = \left(p_i + \frac{\lambda}{d_{i,j}^T a_i} \cdot d_{i,j} \right)^T \cdot x_F$$
$$\pi_y(p_i, d_{i,j}) = \left(p_i + \frac{\lambda}{d_{i,j}^T a_i} \cdot d_{i,j} \right)^T \cdot y_F \tag{3}$$

These coordinates are used as input for the beta paint distribution (Eq. 1). Overall, this projection generates skewed material distributions on the workpiece, even though the beta paint distribution is not skewed.
After this step, the material deposit is scaled by $a(n_j, d_{i,j})$, given in Eq. 4.

$$a(n_j, d_{i,j}) = \begin{cases} \frac{(-d_{i,j})^T \cdot n_j}{||d_{i,j}||_2 \cdot ||n_j||_2}, & (-d_{i,j})^T \cdot n_j > 0 \\ 0, & (-d_{i,j})^T \cdot n_j \leq 0 \end{cases} \tag{4}$$

As the sprayed area increases with increasing spray angle, less material needs to be applied per point as the mass flow remains the same. If the spray angle is equal to or greater than 90°, the material deposit is zero. In addition, we scale the material deposit with the spray duration $\hat{t}_i = \frac{t_{i-1}+t_i}{2}$ and we also consider the distance from the TCP p_i to the point v_j. The final simulation model for determining a material deposit z_j at v_j is given by Eq. 5. The model is visualized in Fig. 2.

$$\begin{aligned} z_j &= \sum_{i=0}^{n} z(v_j, n_j, p_i, \hat{t}_i) \\ &= \sum_{i=0}^{n} \left(\frac{a(n_j, v_j - p_i)}{||v_j - p_i||_2^2} \cdot \hat{t}_i \cdot T(\pi_x(p_i, v_j - p_i), \pi_y(p_i, v_j - p_i)) \right) \end{aligned} \tag{5}$$

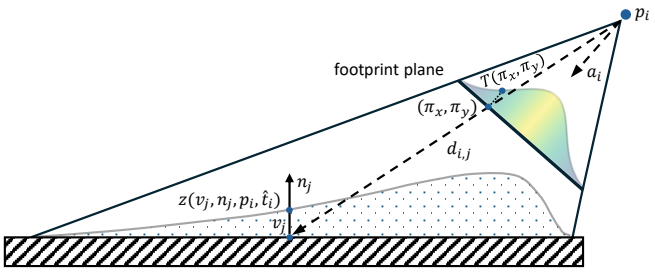

Fig. 2: The material deposit at v_j is determined by projecting v_j onto the footprint plane by using $\pi_x(p_i, d_{i,j})$ and $\pi_y(p_i, d_{i,j})$ (abbreviated as π_x and π_y). These coordinates serve as input to $T(\pi_x, \pi_y)$ to determine the unscaled deposit which is then scaled by further factors to obtain the final deposit $z(v_j, n_j, p_i, \hat{t}_i)$.

3.3 Determination of our Footprint

To determine our default footprint, we sprayed orthogonally with a fixed position and orientation of the spray gun onto a flat surface for two seconds, at a distance of 300 mm, and with $p_r = 5$ bar and $p_f = 0$ bar. The slurry value was set to 1 bar, the pilot air was activated, and the cutter value was set to 3.5 bar. Afterwards, we sampled the spray pattern consisting of fibers and slurry with a resolution of 100 mm^2. The K450 electronic external measuring gauge (Kroeplin Längenmesstechnik, Germany) was used for this measurement. The device has an error of 0.05 mm. The process was repeated three times, and the mean was considered. Fig. 3a depicts the final averaged spray pattern.

To determine the bivariate beta paint distribution (Eq. 1) for our FSP, we fitted the simulation model (Eq. 5) to the averaged spray pattern. We used the Levenberg-Marquardt algorithm, minimizing the mean squared error (MSE). For the footprint plane we choose $\lambda = 50$ mm. Fig. 3b shows the resulting spray pattern when simulated through the fitted footprint. The residuals are depicted in Fig. 3c. Overall, the MSE is 0.017 mm with a standard deviation of 0.107 mm. The parameters of the fitted bivariate beta paint distribution (our default footprint) are listed in the following: $\hat{C} = 1.293\,614\,37 \cdot 10^5$ mm, $\hat{\beta}_1 = 7.84, \hat{\beta}_2 = 7.98, \hat{w}_1 = 26.67$ mm, $\hat{w}_2 = 23.33$ mm.

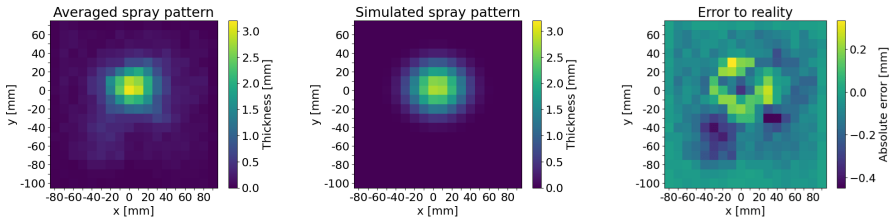

(a) (b) (c)

Fig. 3: We fitted the model (Eq. 5) into our averaged spray pattern (Fig. 3a). The fitted footprint generates the simulated spray pattern (Fig. 3b). The residuals are depicted with a differently scaled color bar for a better visualization (Fig. 3c).

3.4 Determination of the round and flat jet influence

As mentioned, the round jet value p_r and flat jet value p_f influence our default footprint. Therefore, we describe w_1 and w_2 by functions: $w_1 = f(p_r, p_f)$ and $w_2 = g(p_r, p_f)$. To determine these two functions for our FSP, we carried out several experiments with all possible combinations of $p_r \in \{4, 5, 6\}$ bar and $p_f \in \{0, 0.25, 0.5, 0.75\}$ bar. A further change is not useful because the overspray becomes larger, leading to slurry back splash on the robot. This could block the cutting unit of fiber rovings. All other parameters are the same as in Sec. 3.3.

We measured the diameters of all spray patterns and calculated the opening angles of the spray cones in both the x_F- and y_F-direction. We used these angles to determine w_1 and w_2 within the footprint plane. Overall, it resulted in a sampling of the two functions in a rectangular grid, which is why we use bilinear interpolation to determine further values. The results are shown in Fig. 4.

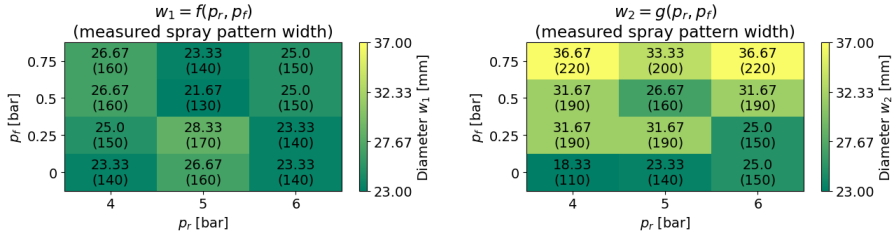

(a) (b)

Fig. 4: We carried out several footprint experiments (Sec. 3.3), but with variation of the round/flat jet to measure the influence on the diameters $w_1 = f(p_r, p_f)$ (Fig. 4a) and $w_2 = g(p_r, p_f)$ (Fig. 4b). These are shown in each cell, with the measured spray pattern size at a spraying distance of 300 mm in brackets.

In Fig. 4a, it is noticeable that w_1 remains relatively constant regardless of p_r and p_f. The fluctuations in the values were probably due to noise. On the one hand this is due to the fact that we only performed each experiment once for a first trend correlation. On the other hand, measuring the diameter is very difficult as it is not possible to identify the boundaries of the spray pattern clearly. In Fig. 4b, the effect of p_r on the diameter w_2 is similar. However, there is a clear tendency for the diameter w_2 to increase as p_f increases.

4 Evaluation and Discussion

We evaluated the model with our real FSP based on a six degree of freedom robot [5] and a meander trajectory size of 300x300 mm^2 to spray a 500x500 mm^2 plate. The trajectory was parallel to the plate at a distance of approximately 430 mm and was traveled at an average speed of 0.16 m/s. The angle between the spray cone axis and the plate was 65°. The round/flat jet was $p_r = 5$ bar and $p_f = 0.25$ bar. The slurry value was set to 1 bar, the pilot air to activated and the cutter value to 3.5 bar. We scanned the deposit using the Shining 3D EinScan Pro HD 3D scanner (Shining 3D Tech Co., Ltd, China) with a scan accuracy of up to 0.045 mm. Afterwards, we determined the real thickness by comparison with a reference scan. The relevant sections of the plate are shown in Fig. 5a for the real deposit and in Fig. 5b for the difference between the simulated to the real deposit. In both figures, the motion started at top left and ended at bottom right, with vertical paths. The robot was positioned at the bottom center.

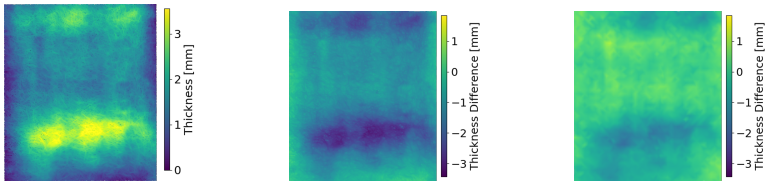

(a) Real thickness (b) Difference (c) Optimized difference

Fig. 5: The difference of the (scaled) simulated thickness (Fig. 5b, 5c) to the real thickness (Fig. 5a) resulting from a meander trajectory is shown here.

The maximum thickness of the plate (Fig. 5a) is 3.56 mm, with an average of 1.6 mm. There are accumulation points at the lower and upper ends of the meander path as the robot's speed decreases and more material is applied. The difference of the simulation to reality (Fig. 5b) is on average -1.24 mm and at maximum -3.43 mm at the accumulation points. This means that too little material is simulated consistently. Therefore, we scaled the simulated thickness to minimize the difference (Fig. 5c). For this, scaling the simulated thickness with a factor of 4.9 is optimal. The maximum deviation is -0.71 mm on average and 1.84 mm at most.

Thus, scaling the deposit results in an error reduction. In order to map this increased mass flow more realistically, the footprint calibration should be carried out with a moving robot. The good results of the calibration (Sec. 3.3) can only be transferred to stationary sprayings. However, as this scaling also introduced an error, FSPs are not entirely represented by this model. For example, we observed that the deposit did not scale linearly with the spray duration, and the pattern diameters w_1 and w_2 increased with the spray duration.

5 Conclusion

In this paper, we contributed the application of a footprint based simulation model to our fiber spraying process (FSP) for short fiber reinforced oxide fiber composites. We used the beta paint distribution for our footprint, which yields good calibration results. The evaluation shows that for a moving robot and a planar workpiece, the application of the model is limited, as too little deposit is simulated. As a result, stationary spray gun calibration is insufficient when spraying is performed during motion. In addition, the model must consider further characteristics of FSPs, like the spray duration's impact on the material deposit and on the spray cone size. Further experiments are needed to evaluate the effect of the compressed air.

Acknowledgement

This work was funded by the Deutsche Forschungsgemeinschaft (DFG, German Research Foundation) - 518255159 (FlexFiber).

References

1. Prashanth S, et al. (2017) Fiber Reinforced Composites - A Review. Journal of Material Science and Engineering, 06(03):341.
2. Erden S, Ho K (2017). Fiber Technology for Fiber-Reinforced Composites. Fiber Technology for Fiber-Reinforced Composites. Woodhead Publishing.
3. Winkelbauer J, et al. (2022) Short fiber spraying process of all-oxide ceramic matrix composites: A parameter study. Int. J. Appl. Ceram. Technol., 20(2): 754-767.
4. Witten E, Mathes V (2023) Der europäische Markt für Faserverstärkte Kunststoffe / Composites 2023. Marktentwicklungen, Trends, Herausforderungen und Ausblicke. AVK e.V.
5. Schmidt E, et al. (2020) Robot-Based Fiber Spray Process for Small Batch Production. Annals of Scientic Society for Assembly, Handling and Industrial Robotics.
6. Schmidt E, Henrich D (2021) Playback Robot Programming Framework for Fiber Spraying Processes. Annals of Scientic Society for Assembly, Handling and Industrial Robotics.
7. Hegels D (2017) Optimierung thermischer Verhältnisse bei der Bahnplanung für das thermische Spritzen mit Industrierobotern. Dissertation, Universität Dortmund.
8. Faserspritzanlagen Wolfangel. https://wolfangel.com/faserspritzanlagen/
9. Faserspritzanlagen BÜFA Composite Systems. https://buefatec.de/product_info.php?products_id=956.
10. Graco FRP Faserspritzanlage. https://www.pultex.de/de/Graco_FRP_Faserspritzanlage/.
11. Robotergesteuerte Faserspritzanlage. https://www.wki.fraunhofer.de/de/fachbereiche/hofzet/profil/technische-ausstattung/Faserspritzanlage.html.
12. Schmidt E, Henrich D (2022) Intuitive Optimization of Kinesthetic Programmed Trajectories for Fiber Spraying. International Conference on Robotics in Alpe-Adria Danube Region.
13. Chen Y, et al. (2017) Paint thickness simulation for painting robot trajectory planning: a review. Industrial Robot: An International Journal, 44(5): 629-63.
14. Conner DC, et al. (2005) Paint deposition modeling for trajectory planning on automotive surfaces. IEEE Trans. Autom. Sci. Eng., 2(4): 381-392.
15. Zhou B, et al. (2014) Off-line programming system of industrial robot for spraying manufacturing optimization. 33rd Chinese Control Conference (CCC).
16. Balkan T, Arikan MAS (1999) Modeling of paint flow rate flux for circular paint sprays by using experimental paint thickness distribution. Mechanics Research Communications, 26(5): 609-617.
17. Arikan MAS, Balkan T (2005) Modeling of paint flow rate flux for elliptical paint sprays by using experimental paint thickness distributions. Industrial Robot: An International Journal, 33(1): 60-66.
18. Zhang Y, et al. (2006) New model for air spray gun of robotic spray-painting. Chinese Journal of Mechanical Engineering, 42(11): 226-233.
19. Xia W, et al. (2010) Paint deposition pattern modeling and estimation for robotic air spray painting on free-form surface using the curvature circle method. Industrial Robot: An International Journal, 37(2): 202-213.
20. Andulkar MV, Chiddarwar SS (2015) Incremental approach for trajectory generation of spray painting robot. Industrial Robot: An International Journal, 42(3): 228-241.
21. Winkelbauer J, et al. (2022) Short fiber-reinforced oxide fiber composites. Int. J. Appl. Ceram. Technol., 19:1136-1147.